Atomistic simulation study of the structure and dynamics of a faceted crystal-melt interface

Dorel Buta* and Mark Asta
Department of Chemical Engineering and Materials Science, University of California Davis, Davis, California 95616, USA

Jeffrey J. Hoyt
Department of Materials Science and Engineering, McMaster University, Hamilton, Ontario, Canada L8S 4L7

(Received 14 May 2008; published 22 September 2008)

A detailed analysis of the structure and dynamics of the crystal-melt interface region in silicon, modeled with the Stillinger-Weber potential, is performed via molecular dynamics simulations. The focus is on the faceted (111) crystal-melt interface, but properties of the rough (100) interface are also determined. We find an intrinsic 10-90 interface width of 0.681 ± 0.001 nm for the coarse-grained density profile at the (111) interface and a 0.570 ± 0.005 nm width at the (100) interface. Coarse-grained profiles of a suitably defined local order parameter are found to show a smaller width anisotropy between (111) and (100) interfaces while the order profiles exhibit a 0.20–0.25 nm shift in position toward the crystal phase relative to the corresponding density profiles. The structural analysis of the layer of melt adjacent to the (111) facet of the crystal finds ordered clusters with average lifetimes of 16 ps, as determined from autocorrelations of time-dependent layer structure factors, and cluster radii of gyration from 0.2 nm for the smallest cells to as large as 1.5 nm.

DOI: 10.1103/PhysRevE.78.031605 PACS number(s): 68.08.−p

I. INTRODUCTION

An important benchmark and key ingredient in the development of theoretical models for the thermodynamic and kinetic properties of crystal-melt interfaces is the equilibrium interfacial structure [1,2]. For atomically rough crystal-melt interfaces, density-functional theories provide direct relationships between the magnitudes and anisotropies of interfacial free energies and mobilities, and the equilibrium widths of suitably defined density profiles (e.g., [3,4]). Additionally, for faceted crystal-melt interfaces, the nature and spatial extent of lateral ordering fluctuations, within the liquid interfacial layers, can be expected to influence the dynamics of terrace nucleation, and step growth kinetics [5]. Recent advances in electron microscopy and x-ray scattering techniques have led to a growing number of experimental studies devoted to the structural properties of solid-liquid interfaces. These studies have demonstrated direct measurements of density profiles, as well as the lateral short-range order in liquid layers adjacent to crystals [2,6–11]. To date, such measurements have focused primarily on studies of heterogeneous solid-liquid interface systems, i.e., systems where the solid and liquid phases have distinctly different compositions. Due to the significant challenges inherent in measuring structural properties for compositionally homogeneous crystal-melt interfaces, experimental data are much more limited in this case, and the most detailed structural information for this important class of solid-liquid interfaces continues to be provided by computer simulations [1,2].

Simulation studies of elemental crystal-melt interface structures have been mainly concerned with model hard-sphere [12] and Lennard-Jones [13,14] systems, as well as a few metal systems modeled by many-body interatomic potentials [4,15] or *ab initio* molecular dynamics [16]. While these studies have provided detailed insights, they have been limited to systems with relatively simple crystal structures (fcc or bcc), where the interfaces are atomically rough, and the properties are weakly anisotropic. By contrast, the understanding of crystal-melt interfaces for more complex crystal structures with associated *faceted* crystal-melt interface orientations, is far less developed. In the current work we employ molecular dynamics simulations in a detailed study of the structural properties of crystal-melt interfaces in silicon, modeled with the Stillinger-Weber (SW) potential [17]. This work extends earlier studies of crystal-melt interfaces in SW Si [18–20], which have demonstrated that the potential correctly reproduces the faceted nature of the (111) interface, and the atomically rough character of the (100) orientation. This previous work thus highlights SW Si as a particularly interesting model system for which the equilibrium structural and dynamical properties of faceted and rough interfaces can be compared for the same underlying interatomic potential.

The present work is motivated in part by our earlier molecular dynamics study of step growth kinetics at (111) vicinal interfaces in SW Si [21]. In the step growth work we obtained values for the step mobilities which are substantially higher than the predictions of classical theories. Following the work of Chernov [3,5], we identified as a potentially important factor contributing to the rapid step kinetics the enhanced crystalline order in the interfacial melt region adjacent to the crystalline terrace. Indeed, in the earlier work of Abraham and Broughton [19,20], the transition from solid to liquid at the (111) facet was determined to be restricted to one layer of melt at the interface, which qualitatively was shown to display an increased degree of ordering due to the presence of the crystalline facet. The current work explores the static and dynamic properties of ordering fluctuations within this (111) interfacial layer in greater detail. The spatial and temporal extent of ordering fluctuations taking place in the transitional layer, as well as adjacent layers, is determined by computing pair distribution functions, structure factors, and time autocorrelation functions of instantaneous

*dbuta@ucdavis.edu

structure factors. In the process, we also perform a more thorough analysis comparing other features of the interface structure for the faceted (111) and atomically rough (100) orientation. We thus extend the early computational studies of (111) and (100) interfaces in SW Si by Landman *et al.* [18] and Abraham and Broughton [19,20]. We go into significantly more detail using new methods of interface analysis [12] together with larger systems and longer simulation times, which enable us to derive a more thorough understanding of the interface structure and dynamics, at a level comparable to that which has been obtained in more recent studies for hard-sphere [12], Lennard-Jones [14], and metal [16] systems.

We continue the presentation in Sec. II by reviewing briefly the method used for preparing the crystal-melt interfaces, already detailed in a previous paper [21]. The various analysis techniques employed are also described in Sec. II. The main results are presented and discussed in Sec. III. A summary of the analysis concludes the report in Sec. IV.

II. COMPUTATIONAL METHOD AND ANALYSIS TECHNIQUES

A. Molecular dynamics simulations

The Stillinger-Weber potential is a classical empirical potential designed to describe the properties of silicon atoms in solid and liquid phases [17]. In addition to two-body forces, the SW potential contains three-body, angular terms, whose main role is to guide the angle between bonds to the value that it takes in the tetrahedral structure of diamond cubic silicon, $\cos\theta=-1/3$. The work of Stillinger and Weber and subsequent studies have shown that the SW potential provides a qualitatively appropriate model for structural and thermodynamic properties of solid and liquid phases of silicon. Classical molecular dynamics (MD) algorithms included in the parallel MD software LAMMPS [22] are employed in constructing and equilibrating crystal-melt interfaces perpendicular to the [111] and [100] directions. The interfaces are set up in a straightforward sequence of steps detailed in a previous publication [21].

Separate bulk crystal and liquid systems are prepared at zero pressure and temperature just below the melting temperature. The two phases are brought into contact and allowed to relax briefly in an ensemble that allows the volume to adjust in the direction normal to the interface (z) while keeping the area of the interface A_{xy} fixed ($NA_{xy}p_zT$ ensemble). In the final stage, the combined solid-melt system reaches equilibrium coexistence under a constant energy and volume (NVE) run. The coexistence temperature (melting temperature) is found to be 1679 K for both the (111) and (100) interfaces. The final size of the simulated systems, expressed as the volume $L_x(\text{nm})\times L_y(\text{nm})\times L_z(\text{nm})$, is $8.19\times 8.19\times 21.32$ for the $z=[100]$ system and $7.72\times 8.02\times 18.63$ for the $z=[111]$ system. In terms of the zero-pressure lattice constant a, the xy cross sections are $15a\times 15a$ for the (100) system and $10\sqrt{2}a\times 6\sqrt{6}a$ for the (111) system. The corresponding numbers of silicon atoms are 72 900 and 59 250, respectively, divided approximately evenly between the coexisting solid and melt phases. Shown in Fig. 1 are cross-sectional snapshots of the interfacial regions of the resulting equilibrated systems for (111) and (100) interfaces; the faceted nature of the flat (111) interface versus the rough structure for (100) is clearly apparent in these snapshots.

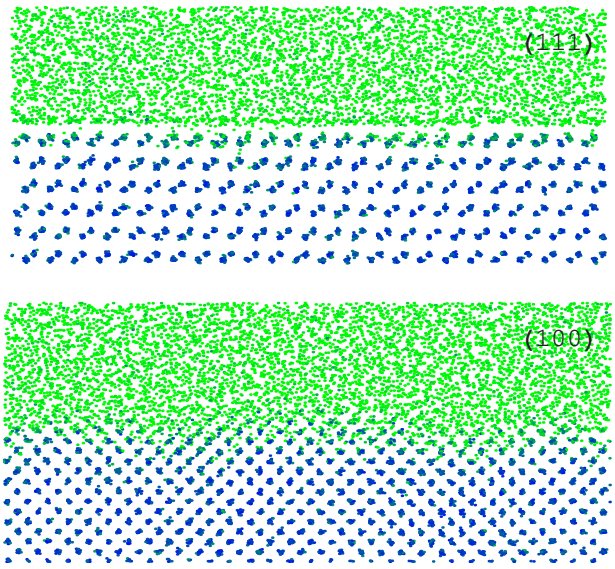

FIG. 1. (Color online) Snapshots of (111) (top) and (100) (bottom) crystal-melt interface regions in silicon. The atom coordinates are projected onto the plane of the page. The viewpoints, as defined by the directions perpendicular to the page, are $(10\bar{1})$ and (010), respectively. The points representing the atoms are colored in proportion to a local order parameter [Eq. (3)]: from blue (dark gray) for an order parameter value of 1 (order) to green (light gray) for a value of 0 (no order).

B. Analysis of density profiles

The density profile across the interface, $n(z)=\langle\rho(\mathbf{r})\rangle_{xy}$, is computed simply as the average number of atoms in discrete slices (bins) of thickness Δz divided by the volume of the slice, $A_{xy}\Delta z$. As discussed in detail by Davidchack and Laird [12], a careful analysis of the density profiles must take into account the broadening of the profile due to equilibrium melting and freezing taking place at the interfaces. This broadening of the profiles is less of a concern in the case of flat (faceted) interfaces, such as the (111) crystal-melt interface in silicon, for which the net motion of the interface due to melting and freezing at equilibrium is negligible. Our approach to dealing with the interface motion relies on calculations of the density profile (and associated profile widths) individually for each configuration in the equilibrium sample. The width of the density profile is then estimated as the average of the widths determined from all configurations.

The average fine scale density profile across two (111) crystal-melt interfaces, without corrections for artificial broadening due to net interface displacements, is displayed in Fig. 2. The bin size is 3 pm and the averaging is over 14 000 snapshots separated by 1 ps. The (100) interface is rough and the broadening effect due to interface motion is expected to be noticeable. The fine-grained profile (bin size

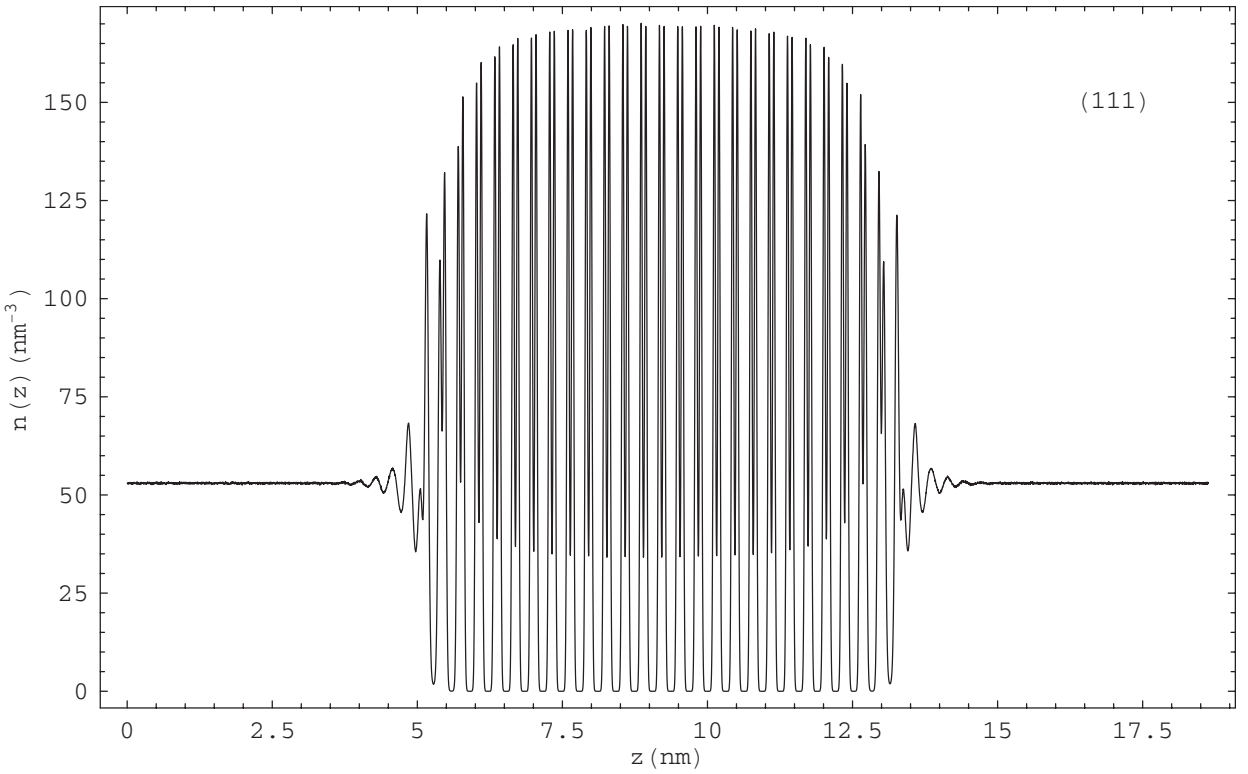

FIG. 2. Fine-scale density profile $n(z)$ in the (111) direction (z coordinate) of the melt-crystal-melt Si system at coexistence. The bin size is 3 pm.

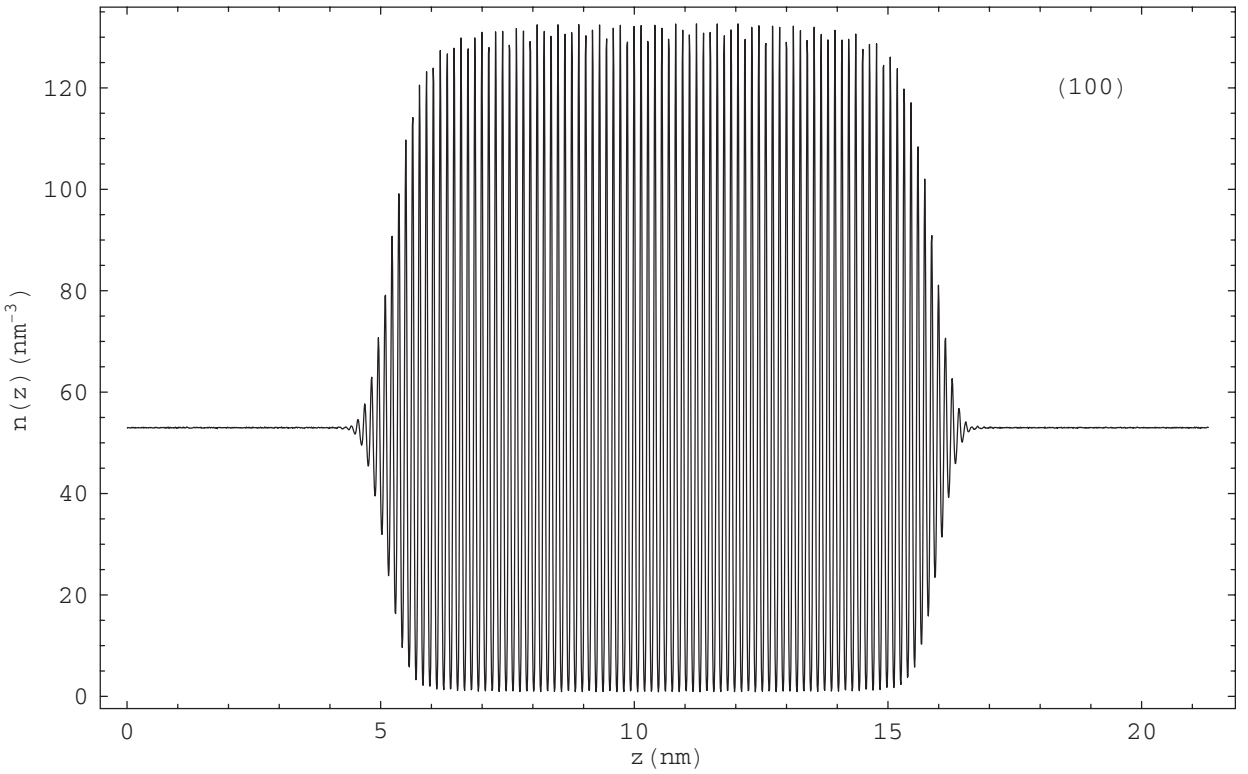

FIG. 3. Fine-scale density profile $n(z)$ in the (100) direction (z coordinate) of the melt-crystal-melt Si system at coexistence. The bin size is 0.01 nm.

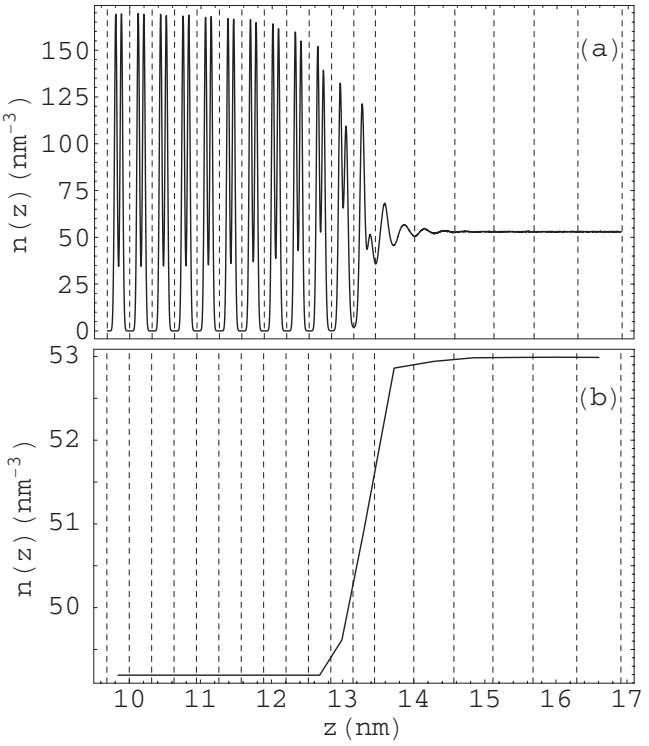

FIG. 4. Illustration of the computation of the coarse-scale density profile $n(z)$ using nonuniform bins that match the crystalline layers and the density oscillations near the interface. (a) shows a portion of the fine-scale density profile at the (111) crystal-melt interface with the coarse-scale bins marked by dashed vertical lines. The coarse-grained profile for the same region is displayed in (b).

10 pm) averaged over 23 500 configurations, covering 23.5 ns, is shown in Fig. 3.

A key parameter in the definition of the density profile $n(z)$, and that of a profile in general, is the bin size Δz. A faithful representation of the spatial density fluctuations in the crystal phase requires a value of Δz much smaller than the period of the fluctuations. For the systems analyzed here values of Δz between 1 and 10 pm have been used, sufficiently small to capture fine density fluctuations on the scale of a few angstroms. The drawback of the fine profile is that it hides the larger-scale features of the crystal-melt interface due to the inhomogeneous nature of the crystal. It is immediately clear, however, that generating profiles with larger bin sizes leads to inconsistent coarse profiles that depend on the choice of bin size. A natural coarse-graining procedure is based on nonuniform bins designed to match the widths of the layers [or bilayers in the case of the (111) interface] in the crystal phase and that of the density fluctuations in the melt. The procedure is illustrated in Fig. 4 where the spacing of the grid lines varies across the interface to match the minima in the averaged fine-grained density profile. The grid lines for the (111) system are positioned to encompass approximate bilayers both in the crystal and in the interface region. An initial guess for the location of the grid lines is refined by finding the minima of the locally smoothed profile. Although the procedure is simple and can be automated, it can become tedious if several profiles have to be analyzed.

Davidchack and Laird [12] devised an alternative solution to the problem of generating coarse-grained profiles based on

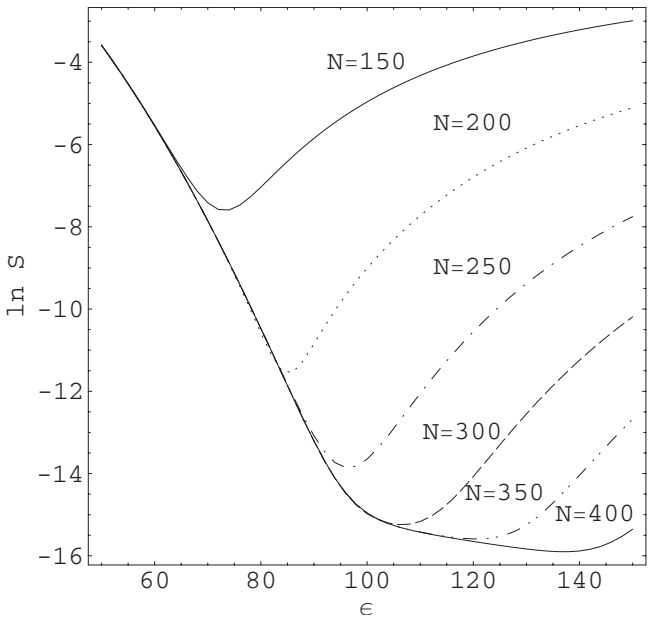

FIG. 5. Logarithm of the smoothness function S computed for filtered profiles obtained from the fine-scale profile of Fig. 2. The six lines correspond to six values of the filter parameter N in the range 150–400. Each line shows a clear minimum in the dependence on the second filter parameter ϵ.

a smoothing algorithm known as finite impulse response (FIR). The FIR method smooths over oscillations in the profile by applying a moving, weighted average over the discrete values of the fine scale profile. With the notation of Davidchack and Laird, the FIR smoothed profile value for bin n, $\bar{f}_n$, becomes

$$\bar{f}_n = \sum_{k=-N}^{N} A \exp(-k^2/\epsilon^2) f_{n+k}, \tag{1}$$

where f_n is the value corresponding to bin n of the fine profile, A is a normalization factor, and N and ϵ are parameters that control the range of the weighted average used for smoothing. While computationally straightforward, the FIR approach still presents the user with a choice for the parameters N and ϵ. Following Davidchack and Laird [12], a smoothness measure of the coarse-grained profile is defined as

$$S = \sum_n (\delta^2 \bar{f}_n)^2, \tag{2}$$

where $\delta^2 \bar{f}_n = \bar{f}_{n+1} + \bar{f}_{n-1} - 2\bar{f}_n$. The choice for N and ϵ is given by the minimization of S. The smoothness measure corresponding to the coarse-graining of the fine-scale density profile of Fig. 2 is shown as a function of ϵ in Fig. 5 for several choices of N. A clear minimum of $\ln S$ can be identified for every N value. The minima of $\ln S$ show a strong dependence on N in the range $N < 250$ but barely change beyond $N = 300$, suggesting an optimal choice $N = 300$ and a corresponding $\epsilon = 106$ as the location of the minimum of S. Applying the FIR coarse-graining procedure with $N = 300$ and $\epsilon = 106$ leads to the density profile displayed in Fig. 6, which

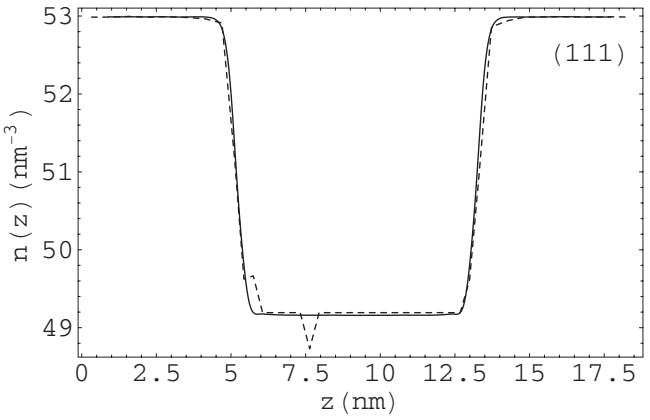

FIG. 6. Coarse-grained density profiles for the melt-crystal-melt system with (111) interfaces: FIR method (solid line) and nonuniform bins (dashed line).

shows good agreement with the profile based on nonuniform bins.

C. Analysis of structural order and dynamics

While the density profiles provide a picture of the distribution of material at the interface, they say nothing about the degree of local order at the interface. The degree of local ordering around each atom can be quantified through a discriminator function (also referred to below as an order parameter) designed to take a value of 0 for an atom in the liquid phase and 1 for an atom that is surrounded by a perfect tetrahedral structure. Given this minor constraint, there is a fair degree of freedom in the choice of a discriminator function. We find one type of discriminator to be particularly effective for the case of the Si crystal structure and its melt. The discriminator is a modified version of the function used by Morris *et al.* [23] for materials with an fcc crystal. Noting that $\exp(i\mathbf{q}\cdot\mathbf{r}_{\mathrm{NN}})=1$ for any $\mathbf{q}$ vector with magnitude $4\pi\sqrt{2}/a$ and orientation along one of the 12 nearest-neighbor directions of the fcc structure and any nearest-neighbor bond vector $\mathbf{r}_{\mathrm{NN}}$ of the diamond structure, we write a discriminator function $\psi(i)$ for atom i as

$$\psi(i)=\left|\frac{1}{ZN_{\mathbf{q}}}\sum_{\mathbf{q}}\sum_{j=1}^{Z}\exp(-i\mathbf{q}\cdot\mathbf{r}_j)\right|^2, \tag{3}$$

where Z is the number of atoms j found in a sphere of radius 0.3 nm surrounding atom i (approximately halfway between the first and second shells of neighbors in the crystal) and $N_{\mathbf{q}}=6$ counts one vector from each of the six pairs of antiparallel $\mathbf{q}$ vectors described above. By design, $\psi(i)=1$ if the atom i has four other atoms positioned at the exact locations of the four nearest neighbors of an atom in a perfect diamond cubic crystal and $\psi(i)\approx 0$ for an atom in the melt phase. Intermediate values of $\psi(i)$, between 0 and 1, cover the various degrees of local order and disorder present in the system. Profiles of the discriminator function are computed in a straightforward manner. Rather than counting the number of atoms in each bin, as is done in computing the density profiles, we sum the discriminator values of all the atoms in a bin. The profile obtained can be thought of effectively as a profile of the density of local tetrahedral bonding across the interface. The lateral structural features of the system in the xy planes parallel to the interface are quantified by two-dimensional (2D) versions of the usual pair distribution function, $g_{2\mathrm{D}}(r)$, and structure factor $S_{2\mathrm{D}}(\mathbf{k})$. These two quantities are computed for crystal layers (bilayers in the case of the [111] interface) and liquid layers in the usual manner (Ref. [24] for example), except that only the x and y coordinates are used in the computations. In other words, the layers are treated as two-dimensional systems by projection onto the xy plane. As described below, this analysis identifies pronounced structural short-range order within the interfacial layers. To probe the dynamics of the order fluctuations in the layers, we employ the autocorrelation function of the layer structure factor, $\mathcal{A}(S_{2\mathrm{D}};t)$, which is computed in accordance with its definition as the ensemble average $\langle[S_{2\mathrm{D}}(\mathbf{k},0)-\langle S_{2\mathrm{D}}(\mathbf{k})\rangle][S_{2\mathrm{D}}(\mathbf{k},t)-\langle S_{2\mathrm{D}}(\mathbf{k})\rangle]\rangle$.

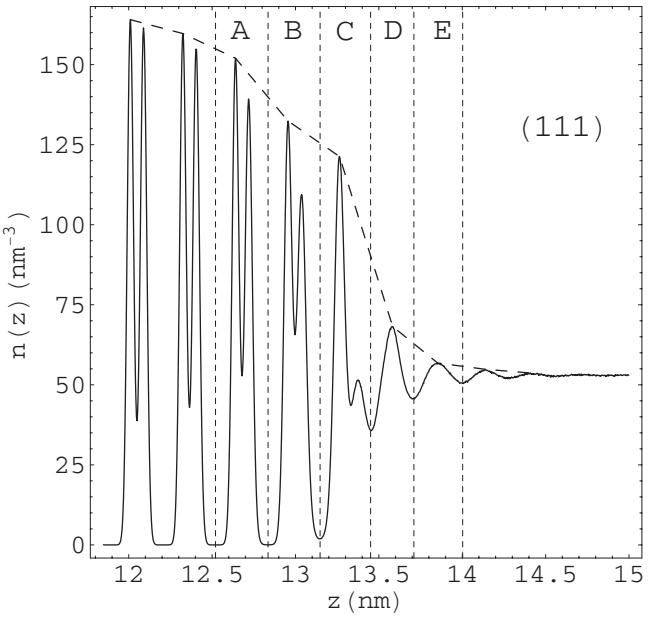

FIG. 7. Closeup of the fine-scale density profile $n(z)$ in the second interface region (crystal-melt) from Fig. 2 with five layers marked by dashed line boundaries. The envelope of the density peaks is sketched with a dashed line (long dashes).

III. RESULTS AND DISCUSSION

A. Density and order parameter profiles

A closeup of the density profile at the interface, shown in Fig. 7, makes clear the "bilayer" nature of the (111) planes in the diamond-cubic crystal structure. It is also noticeable how the two density peaks of a bilayer become slightly broader and overlap more as the interface is approached. This broadening is accompanied by an obvious reduction in the height of the density peaks. The transition to the liquid phase is marked by one last layer exhibiting remnants of a double peak (layer C in Fig. 7), with one well-defined peak and a small secondary peak on the liquid side of the crystal-to-melt transition. The density fluctuations in the liquid decay over a

span of several angstroms away from the interface (four more "layers" can be easily identified after layer *C*). Fitting the dependence of the amplitude of density fluctuations versus coordinate z reveals an exponential decay toward the bulk density of the melt with a decay length of approximately 0.29 ± 0.02 nm.

The spatial extent of the interfacial region is commonly expressed in terms of the 10-90 width of the coarse-grained density profiles. The 10-90 width is defined as the distance over which the density changes from $n_l - 10\%(n_l - n_s)$ to $n_l - 90\%(n - n_s)$ as the interface is traversed from the liquid phase to the solid phase, where n_l and n_s refer to the bulk liquid and solid number densities, respectively. For the average profile of Fig. 6 the 10-90 widths at the two individual interfaces in the periodic simulation cell are essentially equal (the difference is several times smaller than the bin size 3 pm), as expected. Two fitting models are used at the interfaces to compute the 10-90 widths. One model approximates the interface with a hyperbolic tangent function $\{c_1 + c_2 \tanh[c_3(z - c_4)]$, where c_1, c_2, c_3, and c_4 are the fitting parameters$\}$ while the second fit uses the error function $\{c_1 + c_2 \mathrm{erf}[c_3(z - c_4)]\}$. Both models yield excellent fits and 10-90 widths in very good agreement with each other: 0.687 nm for the hyperbolic tangent fit and 0.679 nm with the error function model. It is instructive to compare this value from the coarse-grained density profile with the width of the envelope of the fine scale density profile, as sketched in Fig. 7. Our estimate for the 10-90 width of the profile formed by the local density peaks is only slightly below 1.1 nm, much larger than the 10-90 width of the coarse-grained density profile. This result, that the coarse-grained density shows a width appreciably smaller than the envelope of the fine-scale density profile, is also found in related analyses for hard-sphere and Lennard-Jones alloys [12,14].

An important issue related to the analysis of the density profiles of Fig. 6 is whether they are significantly affected by the net interface motion associated with freezing and melting fluctuations at the interfaces. We address this question by pursuing an alternative averaging procedure to compute the interface widths. The density profiles of individual snapshots are analyzed by means identical to those applied to the average profile; the instantaneous fine density profiles are coarse-grained with the FIR algorithm using the parameters $N=300$ and $\epsilon=106$ determined above. The 10-90 widths calculated for each coarse-grained profile are then averaged to yield an estimate of the 10-90 width: 0.690 ± 0.001 nm if tanh functions are used for fitting the profiles and 0.681 ± 0.001 nm when erf fits are employed. The very slight difference between the latter widths and the widths obtained from the average profile confirms the expectation that the positions of the (111) interfaces show no significant fluctuations due to melting and freezing. An equivalent way of making the same point about the (111) interface is by analyzing the distribution of the interface position, determined in the process of fitting each coarse-grained configuration profile. The standard deviation of the Gaussian distribution corresponding to the (111) interface in Fig. 8 is 0.03 nm, about one-tenth of the bilayer thickness.

In the case of the (100) crystal-melt interface, coarse-graining of the fine scale profile with the FIR method and

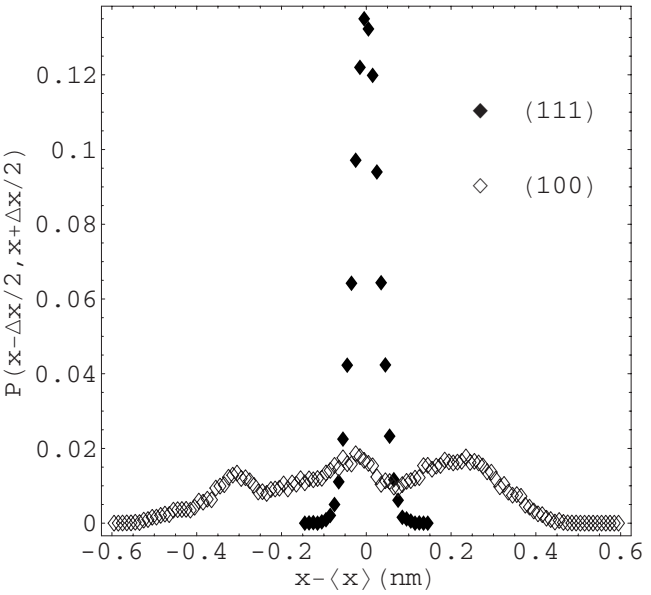

FIG. 8. Probability distribution of the interface position for the (111) (filled symbols) and (100) (open symbols) interfaces. The histogram bin is 0.01 nm.

with nonuniform bins yields consistent results once again, as exhibited by Fig. 9. The parameters used for the FIR profile are $N=40$ and $\epsilon=14$. The 10-90 width of the average density profile is 0.834 nm (from erf fits at the interfaces), significantly larger than the 0.570 ± 0.005 nm value obtained by averaging the widths determined for the individual profiles of each of the 23 500 configurations. The large difference is clearly caused by the significant displacements of the crystal-melt interface position during melting and freezing of atoms at the interface. We check this result by computing the 10-90 width for a density profile that is averaged only over a very small portion of the trajectory (100 configurations out of the total of 23 500) that shows only small displacements of the interfaces. The 10-90 width is roughly 0.56 nm, confirming the result 0.570 ± 0.005 nm from the analysis of instantaneous widths. The distribution of the average location of one interface is plotted in Fig. 8 (open symbols). In contrast with

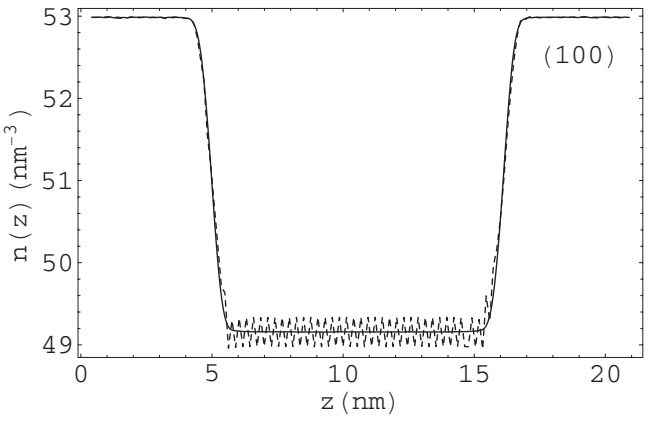

FIG. 9. Coarse-grained density profiles for the melt-crystal-melt system with (100) interfaces: FIR method (solid line) and nonuniform bins (dashed line).

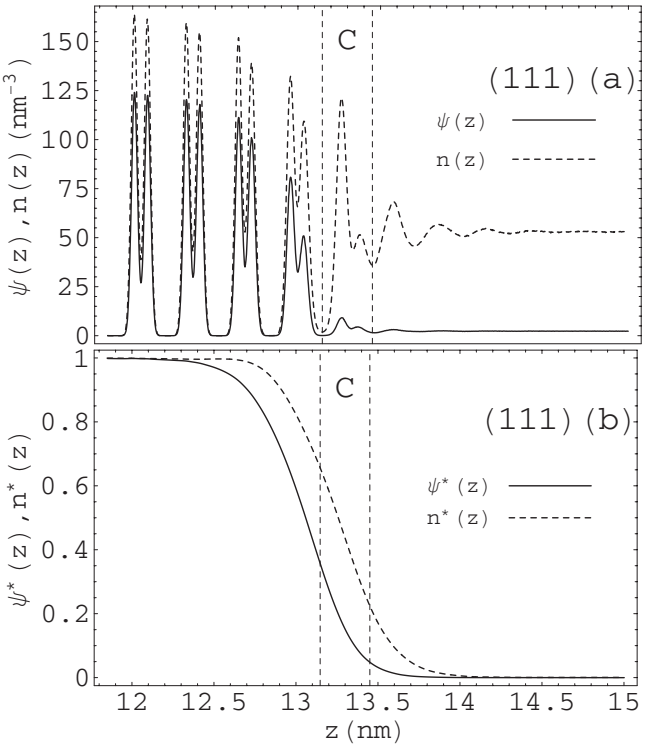

FIG. 10. Fine-scale (a) and smoothed profiles (b) of the density of the local tetrahedral order parameter (solid line) and number density of atoms (dashed line). The pair of vertical grid lines marks the location of layer *C*, as labeled in Fig. 7.

the (111) case, the distribution is broad and has yet to reach a Gaussian shape, even after more than 23.5 ns. The standard deviation is 0.23 nm, equivalent to 1.7 crystal layers.

Complementing the information provided by the density profiles are the profiles of the order parameter defined in Eq. (3). Given the comparable orders of magnitude, it is convenient to plot the order parameter profiles, both the fine-scale and the coarse-grained profiles, with the corresponding density profiles. Figure 10(a) shows such a comparison between the fine-scale profiles of the number density and the order parameter across the (111) interface. For clarity, only a limited region around one crystal-melt interface is shown. In the order-parameter profile the transition layer *C* exhibits again two peaks, but they are sharply smaller than in the adjacent layer of crystal. A direct comparison of the two coarse-grained profiles is shown in Fig. 10(b). The profiles are inverted, scaled, and shifted as needed to obtain the normalized quantities $\psi^*(z)$ and $n^*(z)$ with values in the range [0,1]. The figure shows how the degree of local tetrahedral order starts to diminish as the interface is approached from the solid phase even as the density continues to stay close to its bulk value. The two profiles are shifted relative to each other by 0.2 nm but the difference between their widths is small: an average width of 0.66 nm for the discriminator profile compared to a 0.68 nm average of the widths computed above for the density profile. A similar shift, slightly larger in magnitude at 0.25 nm, is found between the density and local order profiles at the (100) interface. The width of the order-parameter profile in the (100) system is larger than the 10-90 width of the average density profile but by no more than

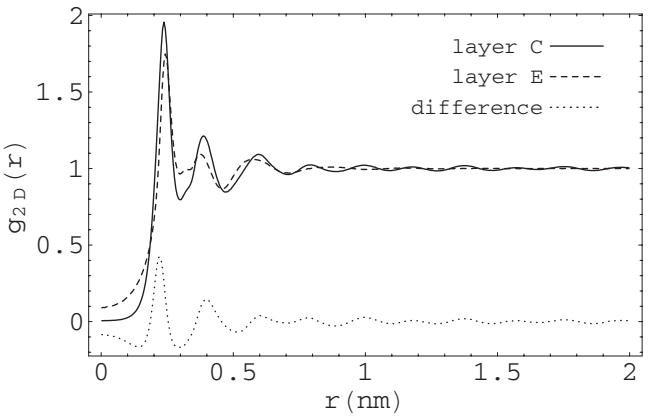

FIG. 11. Two-dimensional pair distribution functions in the *xy* plane for the layers *C* and *E* from Fig. 7. The dotted line represents the difference between the two distribution functions.

0.08–0.10 nm (estimates from the comparison of both the full trajectory average profiles and profiles averaged over the short 100 ps portion of the trajectory, as discussed in the previous paragraph). The observation that the coarse-grained density profile and an order parameter profile can be displaced relative to each other has also been made in a study of the crystal-melt interface in a binary hard-sphere system [25]. Furthermore, if an alternative order parameter, one based on the layer structure factor described below, is used to generate a coarse-grained order profile, a comparable shift relative to the density profile is obtained once again.

B. Lateral ordering within interfacial layers

A more complete picture of the liquid and crystal structure at the interface requires a structural analysis of layers of material within the *xy* plane (parallel to the interface plane). The layers of interest for one (111) interface are defined in Fig. 7. The most interesting layer is layer *C* whose density profile exhibits the double-peak nature of the crystal layers but whose second density peak, closest to the melt, is dramatically reduced in magnitude. The starting point for the analysis is the pair distribution function in the *xy* plane, $g_{2D}(r)$. For clarity, in Fig. 11 we compare first only the pair distribution functions for layer *C* and the melt layer *E*. It is seen that, while there is no long-range order in layer *C*, i.e., the $g_{2D}(r)$ function decays with distance, the short-range order extends over large distances, well above 1 nm. Plotting the difference between the pair distribution functions in the two layers *C* and *E* explicitly (dotted line) makes apparent the large correlation lengths for structural short-range order. Furthermore, the ordering in $g_{2D}(r)$ of layer *C* matches approximately the long-range order in the neighboring crystalline layer *B*, as shown in Fig. 12. The type of pair distribution function that we find in layer *C* is consistent with a system in which clusters of ordered material form and break down in an otherwise liquidlike environment. However, it is clear that a random distribution of such clusters within the layer could not explain the very long range of the order seen in $g_{2D}(r)$. A crucial ingredient is the presence of the "substrate," the crystal bilayer *B*, which restricts the space that is

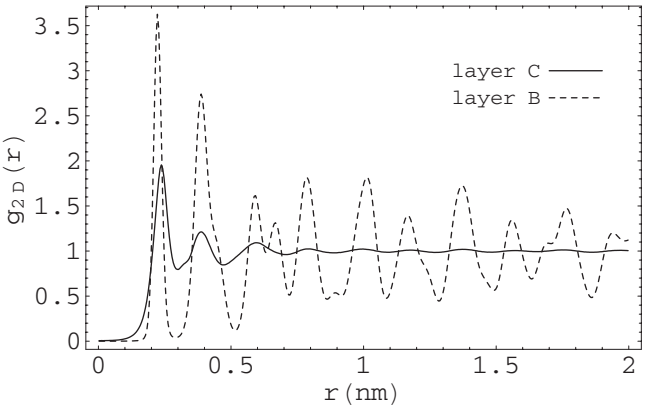

FIG. 12. Two-dimensional pair distribution functions in the *xy* plane for the layers *C* and *B* from Fig. 7.

favorable to the formation of ordered clusters. The effect of this substrate on $g_{2D}(r)$ is then similar to that of an interaction which favors distances between atoms that are commensurate with the translational periodicity of the substrate lattice.

An alternative tool for analyzing the nature of crystalline order in the interfacial layers is a two-dimensional Fourier space representation of the layer structure. We present results for the time-averaged two-dimensional structure factor $S_{2D}(\mathbf{k})$ together with real space snapshots of the four layers *A*, *B*, *C*, and *D* in Fig. 13. The structure factor plots are over a range of wave vectors k_x from $-150\times 2\pi/L_x$ to $150\times 2\pi/L_x$ and k_y from $-150\times 2\pi/L_y$ to $150\times 2\pi/L_y$. The transition from the ordered crystal phase to the liquid is dramatically illustrated by the structure factor of layer *C*, which shows signs of the hexagonal symmetry of the crystalline bilayer for small **k** values and a liquidlike isotropy at larger **k**. All four layers exhibit first peaks (lowest wave vector **k** amplitude peaks) at the six two-dimensional wave vectors with magnitude $|\mathbf{G}_1|=8\pi/(a\sqrt{6})=18.8$ nm^{-1}, where $|\mathbf{G}_1|=|\mathbf{G}_2|$ is the amplitude of the two basis vectors of the 2D reciprocal lattice associated with the hexagonal lattice of the 2D projected crystalline layers. The first peak (ring) of the structure factor in the bulk liquid is shifted toward a larger wave vector magnitude: 23.5 nm^{-1}.

To visualize the nature of the ordering fluctuations discussed above, we present in Figs. 13 and 14 planar snapshots of layers in the (111) interfacial region. In Fig. 14, three snapshots of the layer *C* are shown, corresponding to three configurations with increasing magnitude of the layer structure factor $S_{2D}(|\mathbf{G}_1|,t)$ as follows: 7.1, slightly above the time-averaged value 6.7, in snapshot (a), 9.7 for configuration (b), and the maximum observed value 18.8 for snapshot (c). Configurations (b) and (c) highlight clearly the nature of the crystalline fluctuations occurring in layer *C*. Large ordered clusters can be readily seen in both cases. The largest cluster of Fig. 14(b) consists of approximately 60 atoms and has a radius of gyration of 0.9 nm. In Fig. 14(c) there are as many as 140 atoms in the ordered cluster and the radius of gyration is 1.5 nm. Figure 14(a) presents the same snapshot as Fig. 13: one can identify hexagonal cells with radii of 0.2 nm and slightly larger clusters of ordered atoms in several areas of the projected snapshot, although these clusters are relatively smaller and less clearly distinguished relative to the snapshots (b) and (c). This comparison of the three snapshots of layer *C*, taken at different times, highlights the fact that the structural order in this interfacial layer is highly

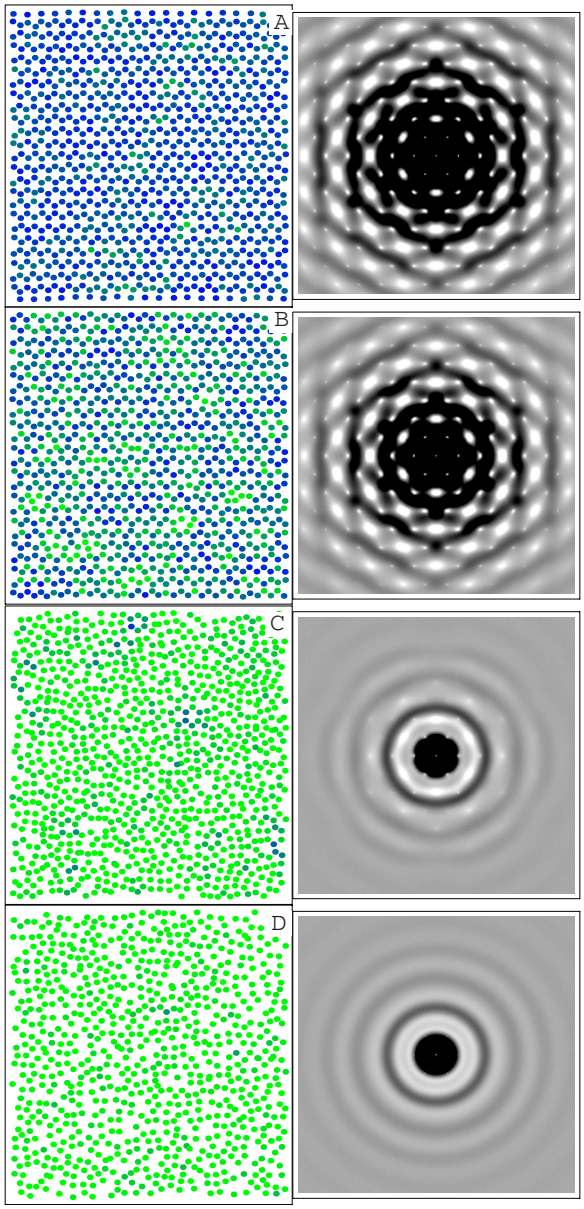

FIG. 13. (Color online) Projected snapshots of the layers *A*, *B*, *C*, and *D* (left column) with the two-dimensional density type plots of time-averaged structure factors (right column) for the corresponding layers. The layers are labeled in Fig. 7. The range of **k** vectors covered in the *x* and *y* directions is $-150\times 2\pi/L_x$ to $150\times 2\pi/L_x$ and $-150\times 2\pi/L_y$ to $150\times 2\pi/L_y$, respectively. For clarity, the linear gray scale of the density plots for the structure factors is restricted to a range of structure factors between 0.5 and 1.5. Values outside this interval are represented by black if smaller than 0.5 and white if larger than 1.5. The disks representing the atoms in the layer snapshots are colored in proportion to the local order parameter of Eq. (3): from blue (dark gray) for an order parameter value of 1 to green (light gray) for a value of 0.

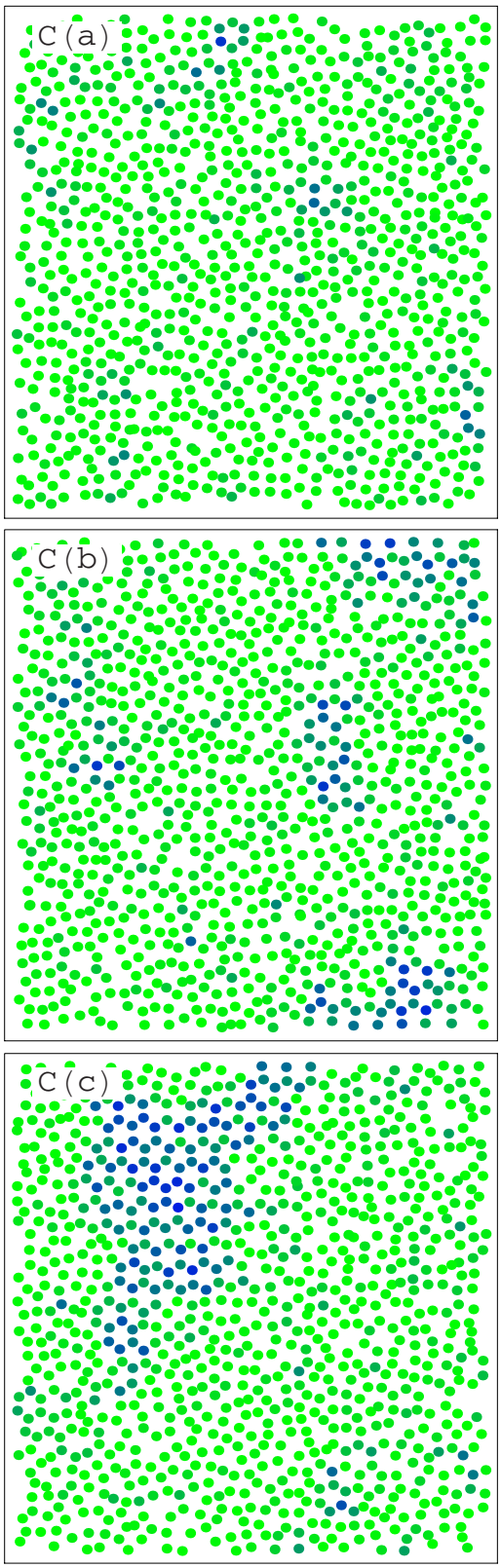

FIG. 14. (Color online) Plan views of layer C in three different snapshots of the (111) crystal-melt system. The three configurations are presented in the order of increasing layer structure factor at the first peak, $S_{2D}(|\mathbf{G}_1|,t)$: 7.1 for configuration (a), 9.7 for (b), and 18.8 for (c). The coloring convention is the same as the one used for the real space snapshots of Fig. 13.

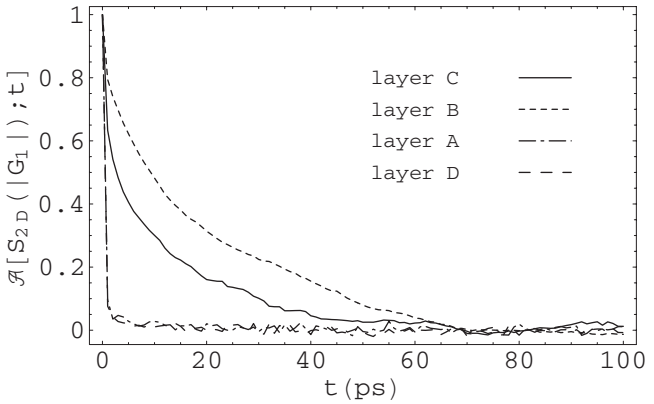

FIG. 15. Normalized autocorrelation function of the two-dimensional structure factor for the projections of layers A, B, C, and D (as labeled in Fig. 7) onto the xy plane. The structure factors are the average of three values computed at three reciprocal space locations with $|\mathbf{k}|=|\mathbf{G}_1|$, the magnitude of the smallest vectors in the reciprocal lattice of the projected crystal layers.

dynamic with clusters forming and breaking up over the time scale of the MD simulation.

To investigate the time scale for the ordering fluctuations, we perform an analysis using the autocorrelation function of the "first peak" structure factor $S_{2D}(|\mathbf{G}_1|,t)$ of the interface layers. For each configuration, $S_{2D}(\mathbf{k},t)$ is averaged over three wave vectors related by the hexagonal symmetry of the crystal layer structure: $\mathbf{k}_1=24\times 2\pi/L_y\hat{\mathbf{y}}$, $\mathbf{k}_2=20\times 2\pi/L_x\hat{\mathbf{x}}+12\times 2\pi/L_y\hat{\mathbf{y}}$, and $\mathbf{k}_3=-20\times 2\pi/L_x\hat{\mathbf{x}}+12\times 2\pi/L_y\hat{\mathbf{y}}$. The structure factors computed in this manner represent a good measure of the degree of translational order in the layers. The results of Fig. 15 show a dramatic increase in the lifetime of order/disorder fluctuations in the two layers at the boundary between melt and crystal, layers B and C, relative to the lack of correlations longer than 1 ps in the adjacent layers. Fitting the long time exponential decay of the autocorrelation functions in layers B and C (for times longer than 5 ps) yields relaxation times of 27 and 16 ps, respectively. The fluctuations are qualitatively different in the two layers: layer B experiences mostly fluctuations representing a "breakdown" (or defects) in its crystalline long-range order, whereas the fluctuations in layer C represent enhanced crystalline short-range order.

IV. SUMMARY AND CONCLUSIONS

We have investigated structural and dynamic properties of equilibrium crystal-melt interfaces in the Stillinger-Weber model of silicon by means of molecular dynamics simulations. The focus is on the (111) and (100) interfaces, which are known to have qualitatively different structures: faceted for (111) and rough for (100). An important consequence of this fundamental difference for the analysis of the simulation is the presence of interface broadening due to melting and freezing of atoms at the rough (100) interface, leading to fluctuations of the interface position and an artificial "broadening" of the interface. Therefore, the intrinsic width of the (100) interface is probed by computing averages of instanta-

neous smoothed density profile widths. The broadening effect due to melting and freezing is shown to be absent for the atomically flat (111) interface, as expected.

The intrinsic width of the (100) interface, defined as a 10-90 width of the coarse-grained density profile, is estimated to equal 0.570 ± 0.005 nm, or the width of approximately four crystal layers; we note that this width is significantly smaller than the value determined directly from the smoothed average density profile, without corrections for broadening: 0.834 nm. The best estimate for the 10-90 width of the smoothed density profile at the (111) interface is 0.681 ± 0.001 nm, larger than the corresponding (100) width, but only slightly larger than the width of two crystal bilayers perpendicular to the [111] direction. The clear dependence of the interface width on orientation is an important result for building coarse-grained models of the crystal-melt interface. The orientation dependence of the interface widths found here, amounting to a roughly 20% anisotropy, stands in contrast to results obtained for fcc crystal-melt interfaces in the hard-sphere model [12], where the comparable anisotropy is roughly an order of magnitude smaller, but matches the (111) vs (100) anisotropy found in Lennard-Jones [14] systems. However, the Lennard-Jones model results show a smaller width for the (111) interface than for the (100) interface: 0.93 and 1.10 nm, respectively (from Ref. [14]).

The change in density taking place at the interface between the crystal and its melt is coupled with a change in the degree of crystalline order. We attempt to quantify two types of order: the local order around an atom in the diamond cubic lattice, whose signature is the tetrahedral arrangement of the four nearest neighbors, and the lateral translational order, which can be found rigorously only in the crystal layers, but can show up over limited areas of other layers parallel to the plane of the interface. The lateral translational order in the interfacial layers is measured both by a two-dimensional pair distribution function and by the amplitudes of the Fourier components of the two-dimensional atom density in the layer, the structure factor. Fine-scale and coarse-grained profiles of the local order parameter are computed and analyzed in the same manner as the number density profiles. For the (111) interface a very small difference is found between the widths of the two types of profiles: the 10-90 width of the order parameter profile is just 0.02 nm smaller than the width of the density profile. However, the two profiles are shifted by approximately 0.2 nm. The displacement between the two profiles means that the local order in the crystal is diminished before the density starts to increase considerably towards the value it takes in the liquid phase, or, equivalently, the decrease in the density of the melt as the interface is approached from the bulk is not matched immediately by a proportional increase in the local tetrahedral ordering of the atoms.

Pair distribution functions computed for the two-dimensional projections of layers at the interface reveal the unique nature of the transition layer between crystal and melt (referred to as layer C above). The long range structure of $g_{2D}(r)$ in layer C is explained by the formation of ordered clusters in registry with the underlying lattice of the crystalline substrate. The Fourier analysis of the same layers reinforces the special character of layer C. The two-dimensional maps $S_{2D}(k_x,k_y)$ of the structure factors show in clear terms the presence of short range order with hexagonal symmetry [consistent with the symmetry of the (111) planes in the diamond cubic structure] in layer C and a virtually perfect isotropic liquid in the next layer of melt. The time autocorrelations of the instantaneous (configurational) structure factor $S_{2D}(\mathbf{k},t)$ computed at the first peaks provide information about the lifetime of the two-dimensional clusters formed in layer C. A long-time exponential decay of the autocorrelation functions is found, with a correlation time of 16 ps in layer C and 27 ps in layer B. The correlation times are much shorter in the adjacent layers (A and D), where the decorrelations take place over less than 1 ps, the time resolution for this analysis. To summarize, the analysis of the structure within the melt interfacial layers establishes the presence of large crystalline clusters, with radii of gyration as high as $1-1.5$ nm and lifetimes larger than 10 ps, in the crystal-melt transition layer (layer C). The results reinforce qualitative arguments constructed in our earlier study of step growth rates for (111) vicinal orientations [21], where it was speculated that the step kinetic coefficients are significantly enhanced by the order in the melt layer that lies on top of the terrace provided by the growing crystal.

ACKNOWLEDGMENTS

The research was supported by the U.S. Department of Energy, Office of Basic Energy Sciences, through Grant No. DE-FG02-06ER46282, and the Computational Materials Science Network. This work used resources of the National Energy Research Scientific Computing Center, which is supported by the Office of Science of the U.S. Department of Energy under Contract No. DE-AC02-05CH11231.

[1] B. B. Laird and A. D. J. Haymet, Chem. Rev. (Washington, D.C.) **92**, 1819 (1992).
[2] W. D. Kaplan and Y. Kauffmann, Annu. Rev. Mater. Res. **36**, 1 (2006).
[3] L. V. Mikheev and A. A. Chernov, J. Cryst. Growth **112**, 591 (1991).
[4] K.-A. Wu, A. Karma, J. J. Hoyt, and M. Asta, Phys. Rev. B **73**, 094101 (2006).
[5] A. A. Chernov, J. Cryst. Growth **264**, 499 (2004).
[6] S. H. Oh, Y. Kauffmann, C. Scheu, W. D. Kaplan, and M. Ruhle, Science **310**, 661 (2005).
[7] S. E. Donnelly, R. C. Birtcher, C. W. Allen, I. Morrison, K. Furuya, M. Song, K. Mitsuishi, and U. Dahmen, Science **296**, 507 (2002).
[8] J. M. Howe and H. Saka, MRS Bull. **29**, 951 (2004).
[9] H. Saka, K. Sasaki, S. Tsukimoto, and S. Arai, J. Mater. Res.

20, 1629 (2005).
[10] H. Reichert, O. Klein, H. Dosch, M. Denk, V. Honkimaki, and T. Lippman, Nature (London) **408**, 839 (2000).
[11] M. F. Reedijk, J. Arsic, F. K. de Theije, M. T. McBride, K. F. Peters, and E. Vlieg, Phys. Rev. B **64**, 033403 (2001).
[12] R. L. Davidchack and B. B. Laird, J. Chem. Phys. **108**, 9452 (1998).
[13] J. Q. Broughton, A. Bonissent, and F. F. Abraham, J. Chem. Phys. **74**, 4029 (1981).
[14] H. E. A. Huitema, M. J. Vlot, and J. P. van der Eerden, J. Chem. Phys. **111**, 4714 (1999).
[15] E. T. Chen, R. N. Barnett, and U. Landman, Phys. Rev. B **40**, 924 (1989).
[16] B. J. Jesson and P. A. Madden, J. Chem. Phys. **113**, 5935 (2000).
[17] F. H. Stillinger and T. A. Weber, Phys. Rev. B **31**, 5262 (1985).
[18] U. Landman, W. D. Luedtke, R. N. Barnett, C. L. Cleveland, M. W. Ribarsky, E. Arnold, S. Ramesh, H. Baumgart, A. Martinez, and B. Khan, Phys. Rev. Lett. **56**, 155 (1986).
[19] F. F. Abraham and J. Q. Broughton, Phys. Rev. Lett. **56**, 734 (1986).
[20] F. F. Abraham and J. Q. Broughton, J. Cryst. Growth **75**, 613 (1986).
[21] D. Buta, M. Asta, and J. J. Hoyt, J. Chem. Phys. **127**, 074703 (2007).
[22] S. J. Plimpton, J. Comput. Phys. **117**, 1 (1995); http://lammps.sandia.gov/index.html
[23] J. R. Morris and X. Song, J. Chem. Phys. **119**, 3920 (2003).
[24] M. P. Allen and D. J. Tildesley, *Computer Simulation of Liquids* (Oxford University Press, Oxford, 1987).
[25] R. Sibug-Aga and B. B. Laird, Phys. Rev. B **66**, 144106 (2002).